Flood forecasting in large karst river basin by coupling

PERSIANN CCS QPEs with a physically based distributed

hydrological model

Ji Li[1]*, Daoxian Yuan[1,2], Jiao Liu[3],Yongjun Jiang[1], Yangbo Chen[4], Kuo Lin Hsu[5], Soroosh Sorooshian[5]

1. School of Geographical Sciences of Southwest University, Chongqing Key Laboratory of Karst Environment, Chongqing, 400715,China

2. Karst Dynamic Laboratory , Ministry of Land and Resources , Guilin 541004 , China

3. Chongqing Hydrology and Water Resources Bureau, Chongqing, 401120 ,China

4. Department of Water Resources and Environment, Sun Yat-sen University, Guangzhou 510275, China

5. Center for Hydrometeorology and Remote Sensing, Department of Civil and Environmental Engineering, University of California, Irvine

 Irvine, California

*Correspondence: Ji Li (445776649@qq.com)

Abstract.

22   There is no long-term meteorological or hydrological data in karst river basins to a large
23   extent. Especially lack of typical rainfall data is a great challenge to build a hydrological
24   model. Quantitative precipitation estimates (QPEs) based on the weather satellites could offer
25   a good attempt to obtain the rainfall data in karst area. What's more, coupling QPEs with a
26   distributed hydrological model has the potential to improve the precision for flood forecasting
27   in large karst watershed. Precipitation estimation from remotely sensed information using
28   artificial neural networks-cloud classification system (PERSIANN-CCS) as a technology of
29   QPEs based on satellites has been achieved a wide research results in the world. However,
30   only few studies on PERSIANN-CCS QPEs are in large karst basins and the accuracy is
31   always poor in practical application. In this study, the PERSIANN-CCS QPEs is employed to
32   estimate the hourly precipitation in such a large river basin-Liujiang karst river basin with an
33   area of 58,270 km^2. The result shows that, compared with the observed precipitation by rain
34   gauge, the distribution of precipitation by PERSIANN-CCS QPEs has a great similarity. But
35   the quantity values of precipitation by PERSIANN-CCS QPEs are smaller. A post-processed
36   method is proposed to revise the PERSIANN-CCS QPEs products. The result shows that
37   coupling the post-processed PERSIANN-CCS QPEs with a distributed hydrological model-
38   Liuxihe model has a better performance than the result with the initial PERSIANN-CCS
39   QPEs in karst flood simulation. What's more, the coupling model's performance improves
40   largely with parameter re-optimized with the post-processed PERSIANN-CCS QPEs. The
41   average values of the six evaluation indices including Nash–Sutcliffe coefficient has a 14%
42   increase, the correlation coefficient has a 14% increase, process relative error has a 8%
43   decrease, peak flow relative error has a 18% decrease, the water balance coefficient has a 7%
44   increase, and peak flow time error has 25 hours decrease, respectively. Among them, the peak
45   flow relative error and peak flow time error have the biggest improvement, which are the
46   greatest concerned factors in flood forecasting.The rational flood simulation results by the
47   coupling model provide a great practical application prospect for flood forecasting in large
48   karst river basins.

49   **Key words**:Quantitative precipitation estimates /QPEs, Precipitation Estimation from Remotely
50   Sensed Information Using Artificial Neural Networks-Cloud Classification System/ PERSIANN-
51   CCS, Liujiang karst river basin , Liuxihe model, Flood forecasting

1 Introduction

53   The highly anisotropic karst water-bearing media and intricate hydraulic conditions make
54   the karst flood process exhibit significant differences in time and space, which led to the
55   laminar flow and turbulent flow transmute into each other in karst areas, and the flood events
56   in karst river basins are more complicated compared with that of in non-karst area(Ford and
57   Williams,2007;Goldscheider and Drew,2007).This makes it difficult to precisely simulate

58 and forecast the karst flood process based on a hydrological model in mechanism. It is a
59 common practice that the karst water-bearing media should be simplified before build a
60 model. For example, making karst river basin as a multiple and nested spatial structure;
61 making the underground river as the intelligible river system in the model; cave as the
62 anisotropic medium with a large vertical infiltration coefficient and porosity but small
63 specific yield. Even so, it is still hard to quantify the spatial structure of the karst water-
64 bearing media with a physics-mathematics model. And the karst flood simulation results
65 usually have some errors that could not be ignored, which is the main problem in flood
66 forecasting in karst river basins(Kovacs and Perrochet,2011).

67   Because the dynamic change of karst hydrological process and the hydraulic conditions of
68 underlying surface are complicated and non-linear in karst area, which makes it hard to obtain
69 the hydrogeology parameters, such as specific yield, hydraulic conductivity and aquifer
70 transmissivity and so on. With the rapid development of remote sensing, GIS technology and
71 hydrogeology, the technology of field work including the tracer tests (Birk et
72 al.,2005;Doummar et al.,2012) and infiltration tests have made a significant progress.
73 However, it is still a challenge to accurately simulate the laws of motion of the karst
74 hydrological process in the karst water-bearing media with these experimental tests. So the
75 traditional methods such as lumped hydrological models are not suitable for flood forecasting
76 in karst area(Hartmann et al.,2013). Compared with the performance of lumped
77 hydrological models, the physically based distributed hydrological models (PBDHMs) have
78 some advantages for karst flood forecasting in mechanism. The PBDHMs divide the whole
79 karst river basin into a series of small grid units named karst sub-streams, which could reflect
80 the real rules of hydrological process and karst development characteristics precisely.
81 Therefore, it has a great application potential to improve the karst floods simulation and
82 forecasting capability (Ambroise et al., 1996). Many PBDHMs have been proposed since the
83 blueprint of the PBDHMs published by Freeze and Harlan (1969). The first full PBDHM is
84 regarded as the SHE model published in 1987(Abbott et al., 1986a, b). Shustert and White
85 (1971) used the PBDHM as an attempt in karst area, in their research, the dissolved carbonate
86 species were analyzed in the waters of 14 carbonate springs in the Central Appalachians. And
87 these springs were classified into diffuse-flow feeder-system types and conduit feeder-system
88 types. The PBDHMs have been achieved many good research results in karst area
89 (Atkinson,1977; Quinlan and Ewers,1985;Quinlan et al.,2011;Duan and Miller,1997;
90 Ren,2006;Liu et al.,2013;Zhang et al.,2007).

91   Since the regulation and storage capacity of the karst water-bearing media are weak.
92 When the accumulated rainfall exceeds the maximum drainage capacity of the channel during
93 a heavy rain storm, then the karst immersion-waterlogging hazard is much more likely to
94 appear in this situation. And the hazard will become more and more serious with the
95 intensification of global extreme weather events. So some effective measures need to be taken

96   to reduce the flood losses. For example, simulating and forecasting the karst flood process

97   reliably with a PBDHM effectively, it is an important non-project measure for flood control.

98   However, there is no enough rain gauges as well as the long-term meteorological or

99   hydrogeological data to build a PBDHM in karst river basin where belongs to ungauged basin.

100   Prediction in ungauged basins (PUB) is the theme of international hydrological decade, the

101   core of which is runoff calculation (Li and Ren, 2009). Therefore, it is more difficult to

102   forecast the flood events in karst river basin compared with that of in non-karst area. How to

103   solve the problem of rainfall source is a key factor of the current karst flood forecasting. The

104   quantitative precipitation estimates /QPEs, especially the satellite QPEs technology brings the

105   possibility to obtain the reasonable rainfall data in karst area. But the current application of

106   the QPEs is not mature enough, which makes the accuracy of QPEs as well as the effect of

107   karst flood simulation and forecasting are not so good.

108   The developed numerical weather prediction model in the past decades provided a

109   reasonable and accurate QPEs product in karst area. The current mainstream QPEs including

110   the weather radar QPEs (Delrieu et al.,2014; Rafieei et al.,2014; Faure et al.,2015), satellite

111   QPEs and radar merging satellite QPEs (Stenz, 2014; Bartsotas et al.,2017; Goudenhoofdt and

112   Delobbe,2009; Wardhana et al.,2017), Precipitation estimation from remotely sensed

113   information using Artificial Neural Networks/PERSIANN QPEs (Soroosh et al.,2000; Hirpa

114   et al.,2010; Romilly, 2011;Yang et al.,2007), PERSIANN-Climate Data Record/PERSIANN-

115   CDR (Ashouri et al., 2014; Liu et al., 2017; Tan and Santo,2018; Hussain et al., 2018), and

116   PERSIANN-Cloud Classification System/PERSIANN-CCS (Yang et al., 2004,2007;

117   Moradkhani and Meskele, 2010). The research on the QPEs products by meteorological

118   satellites has become a hotspot in rainfall prediction (Hu et al., 2013).

119   Although many scholars at home and abroad have done a lot of research with the QPEs

120   technology, also achieved many accepted results. However, there are considerable uncertainty

121   exists in the application, which makes the precision of the QPEs is low and the precipitation

122   result by the QPEs is not satisfactory. Two effective measures could reduce the uncertainty of

123   the QPEs results in karst area. One is to match the appropriate resolution of the model.

124   Because the resolution can affect the result of the QPEs directly: if the resolution is too low,

125   then the grid units divided are coarse, which causes a considerable error in rainfall estimates;

126   if the resolution is too high, the meteorological model structure is complicated and unstable.

127   Furthermore, the requirement of computation resources will increase exponentially with the

128   raise of the model spatial resolution (Chen et al., 2017), which leads to huge calculation and

129   low efficiency. So the appropriate model spatial resolution is extremely important for the

130   results of QPEs. And the other is the current technology of QPEs still has some systematic

131   errors existed due to the uncertainties in structure and mathematical algorithm. For this reason,

132   the results of QPEs compared with the observed precipitation by rain gauge have some
133   relative errors, which causes the karst flood simulation results by the coupling model
134   (coupling QPEs with a PBDHM) have uncertainties that affect the model's performance
135   largely. So the results of initial QPEs could not be used directly to build the coupling model.
136   In this study, a post-processed method is employed to revise the PERSIANN-CCS QPEs
137   products, which makes the result of QPEs more credible and receivable.
138   There are many researches on PERSIANN-CCS QPEs (Yang et al 2007) at present. But
139   most of them have been used in small non-karst watersheds. In this study, the PERSIANN-
140   CCS QPEs is employed to estimate the rainfall data as an attempt in such a large karst river
141   basin -Liujiang Karst River Basin (LKRB) with an area of $5.8*10^4 km^2$ in Guangxi province,
142   China. Watershed flood forecasting relies on a PBDHM for a computation tool, while the
143   precipitation is the model's driving force (Li et al., 2017). It has the potential to improve the
144   accuracy of karst flood forecasting by coupling PERSIANN-CCS QPEs with a PBDHM. And
145   the PBDHM in this paper is Liuxihe model(Chen,2009).The spatial resolution of Liuxihe
146   model for LKRB is 200m*200m. And the PERSIANN-CCS QPEs products that the spatial
147   resolution is 0.04 °*0.04 °scale and time interval is 30 minutes are employed to estimate the
148   precipitation results for LKRB. The resolution of the PERSIANN-CCS QPEs must be
149   downscaled to the same size as Liuxihe model before building the coupling model. The
150   PERSIANN-CCS QPEs products after post-processed could offer the high-precision
151   precipitation results for LKRB where lack of enough rain gauges. It can largely improve the
152   model performance by coupling the post-processed PERSIANN-CCS QPEs with Liuxihe
153   model. A modified PSO algorithm (Chen et al., 2016) is used to optimize the coupling model
154   parameters in this paper, which could control the uncertainty of the parameter passing.

155   **2 Methodology**

156   **2.1 PERSIANN-CCS QPEs**

157   The original PERSIANN system (Hsu et al., 1999) was based on geostationary infrared
158   imagery and later extended to include the use of both infrared and daytime visible imagery,
159   which is an automated system for precipitation estimation from remotely sensed information
160   using artificial neural networks .The system for rainfall estimation under development at The
161   University of Arizona and gets constantly stronger with the improvement of the technology
162   (Soroosh et al.,2000). The fundamental algorithm of PERSIANN system is based on a neural
163   network. And the network parameters could be optimized by an adaptive training
164   characteristic, which makes the precipitation could be estimated from geosynchronous
165   satellite at any time and place.
166   The Precipitation Estimation from Remotely Sensed Information using Artificial Neural
167   Networks-Cloud Classification System /PERSIANN-CCS(Yang et al., 2004; Hsu et al., 2007)
168   is a patch-based cloud classification and rainfall estimation system from low Earth-orbiting

169   and geostationary satellites by using pattern recognition technology and computer imaging

170   technology (Yang et al.,2007). Satellite-based precipitation retrieval algorithms use

171   information ranging from visible (VIS) to infrared (IR) spectral bands of Geostationary Earth

172   Orbiting (GEO) satellites and microwave (MW) spectral bands (Hsu et al., 2007).

173   The QPEs products of PERSIANN-CCS has been generated precipitation estimates at

174   resolution 0.04 °*0.04 °scale and time interval 30 minutes since 2000. The output of

175   PERSIANN-CCS QPEs has been downscaled at 200m*200m as the same spatial resolution as

176   Liuxihe model in LKRB. The hourly precipitation data of the PERSIANN-CCS QPEs are

177   collected and compared with the precipitation observed by rain gauges.

178   Rainfall estimation from the PERSIANN-CCS consists as the follow steps (Hsu, 2007):

179   (1) IR cloud image segmentation, (2) Characteristic extraction from IR cloud patches, (3)

180   Patch characteristic classification, (4) Obtain the rainfall estimation results of QPEs products,

181   (5) Evaluate and revise the results of QPEs products.

182   In this paper, the PERSIANN-CCS QPEs real-time data used in LKRB from the current

183   version of PERSIANN-CCS are available and downloadable online

184   (http://hydis8.eng.uci.edu/CCS/).

185   2.2 Liuxihe model

186   Liuxihe model proposed by Yangbo Chen (Chen, 2009)of Sun Yat-Sen University, China

187   is employed as the fully distributed hydrological model in this study, which is a physically

188   based distributed hydrological model(PBDHM)mainly for catchment floods simulating

189   and forecasting(Chen et al., 2011, 2016,2017; Li et al., 2017). Liuxihe model earn its name

190   by first successful application in Liuxihe catchment, Guangdong province, China. There are

191   three layers vertically, including the canopy layer, the soil layer and the underground layer in

192   the model and the whole catchment is divided into a great number of grid cells horizontally

193   by using the DEM, which are treated as a uniform basin, and the elevation, land cover type,

194   soil type, and other model elements including rainfall-runoff, evapotranspiration and so on are

195   calculated on the uniform basin. All cells are categorized into three types, namely hill slope

196   cell, river cell and reservoir cell.

197   An improved PSO algorithm (Chen et al., 2016) is employed to optimize the model

198   parameters in this study, which can make the model's performance much better in flood

199   forecasting in karst river basins. The observed meteorological, hydrological data and the

200   development conditions of the karst underground river are used to optimize the model

201   parameters. The terrain property data like the DEM, land use type and soil type can be

202   downloaded freely from an open access databases on the website. The model is validated by

203   observed karst flood events. All these factors of the model are physically based and rational to

204   truly reflect the underlying surface of the karst basin. So it implied Liuxihe model could be

205   used for real-time flood forecasting in karst river basins.

2.3 The improvement of the Karst hydrological model

Liuxihe model has been applied successfully for floods forecasting in many river basins. However, all these basins are non-karst areas. This is the first time the model is used in karst river basin as an attempt in this study. And the structure of the model should be improved to suit the karst basins. So some effective measures should be taken before building the model. Firstly, simplify the karst water-bearing media, including making karst basin as a multiple and nested spatial structure, underground river as the intelligible channel system in the model, cave as the anisotropic medium with a large vertical infiltration coefficient and porosity but small specific yield, and fault as the anisotropic medium with a vertical, large infiltration coefficient and specific yield. Secondly, the whole karst river basin will be divided into many small karst sub-basins by the theory of distributed hydrological model. Furthermore, the karst sub-basins will be divided into many karst hydrology respond units (KHRUs), which are generally independent of each other. The whole karst hydrological process including the storage and regulation process of the epikarst zone, the spatial interpolation of the precipitation, evapotranspiration and rainfall-runoff are all calculated on the KHRU. After that, these hydrological processes will be summarized in the karst sub-basins. Then the outlet flow will be formed through the river confluence among each karst sub-basin from upstream to downstream. Such a multi-structure distributed hydrological model could utilize various scale information effectively and make the best use of the observed meteorological, hydrological and geological data.

The whole karst river basin is composed by many small karst sub-basins, then the karst sub-basins will be divided into many KHRUs. And each KHRU has its own model characteristics such as the meteorological and hydrological characteristics as well as the karst development characteristics in this study. The KHRU is proposed to describe the spatial variation of the karst sub-basins. And make sure that the differences within the KHRUs are smaller than of among the KHRUs. Then the KHRU is divided into five layers vertically: the canopy layer, the soil layer, the epikarst zone, the bedrock and the underground river. The sketch map of the KHRU is as follow:

The structure of the KHRU(Ren,2006)   b. The photograph of the three-dimensional

space structure of the KHRU

Figure 1. Sketch map of the KHRU

In Figure 1.b, the three-dimensional space model of the KHRU in Liujiang Karst River Basin(LKRB) is built in the laboratory to better understand how groundwater move in the karst media and convert mutually with the surface river. Then the hydrological model could be built more visualized through this way.

242   In order to satisfy the applicability of the model in karst area, the epikarst zone as a

243   distinctive structure of the KHRU is considered carefully in the model. An exponential decay

244   equation is used to calculate the regulation and storage process of surface karst zone. The

245   linear reservoir model is employed to describe the regulation process of the superficial karst

246   fissure system. And the Muskingum routing method is used to calculate the convergence

247   process of the karst underground river that will be summarized and converge to drainage

248   outlet through the underground river system.

249   The karst hydrological process of the epikarst zone could be divided into rapid fissure flow

250   and slow fissure flow. When the precipitation falls to the surface karst zone, it will fill the

251   pores of the macro crack firstly. After all the pores are full-filled, means the macro crack is

252   saturated. This part of saturated water content named rapid fissure flow will go directly into

253   the underground river through the macro crack, and ignore the regulation and storage

254   hydrological process of the macro crack in this study. The rest of the water content will enter

255   the tiny pores in the surface karst zone, and the water content of rapid fissure flow could be

256   described as the following equation:

257 $$SW_{epi} = Q_{\mathrm{inf}} - V_{crk} \qquad (1)$$

258   Where SW_{epi} is the water content of the rapid fissure flow in the epikarst zone,

259   Q_{inf} is the infiltration water content, and V_{crk} is the water content in the macro crack.

260   The slow fissure flow in the epikarst zone is calculated by an exponential decay

261   equation (Ren, 2006):

262 $$\begin{cases} W_{sep} = W_{epi}\left(1 - \exp\left(\dfrac{-\Delta T}{TT_{\mathrm{perc}}}\right)\right) \\ W_{epi,\ t+1} = W_{epi,t} + SW_{epi,t+1} - W_{sep,t+1} \qquad (2) \\ TT_{\mathrm{perc}} = \dfrac{SAT_{epi} - FC_{epi}}{K_{epi}} \end{cases}$$

263   Where W_{sep} is the water content from the epikarst zone to the underground river, W_{epi} is the

264   current water content of the epikarst zone, ΔT is the simulation time-step, TT_{perc} is the

265   attenuation coefficient, SAT_{epi} is the saturation water content of the epikarst zone, FC_{epi} is

266   field capacity of the epikarst zone, and K_{epi} is the saturated hydraulic conductivity of the

267   epikarst zone.

268   The linear reservoir model is employed to calculate the regulation process of the superficial

269   karst fissure system, and the base discharge is calculated by the hydraulic gradient of the KHRU

270   (Neitsch et al.,2000) :

271

272
$$
\begin{cases}
Q_{gw} = 8000 \dfrac{K_{epi} h_{wtbl}}{\left(L_{gw}\right)^2} \\
Q_{gw,i} = Q_{gw,i-1} \exp\left(-a_{gw}\Delta t\right) + W_{rchrg}\left[1 - \exp\left(-a_{gw}\Delta t\right)\right] \\
W_{rchrg,i} = W_{seep}\left[1 - \exp\left(-\dfrac{1}{\delta_{gw}}\right)\right] + W_{rchrg,i-1} \exp\left(-\dfrac{1}{\delta_{gw}}\right)
\end{cases}
\tag{3}
$$

273   Where Q_{gw} is the base discharge, $Q_{gw,i}$ and $Q_{gw,i-1}$ is the supplies quantity of the base

274   discharge that converge to the karst conduit or underground river on the i and (i-1) day

275   respectively, K_{epi} is the saturated hydraulic conductivity of the epikarst zone, h_{wtbl} is the

276   hydraulic gradient, L_{gw} is the length of the KHRU, a_{gw} is the depletion coefficient of the base

277   discharge, ΔT is the simulation time-step(day), $W_{rchrg,i}$ is the supplies quantity of the aquifer

278   on the i day(mm/d), W_{seep} is the water flux through the bottom of the soil profile into the

279   underground aquifer on the i day(mm/d), δ_{gw} is the delay time of the supplies(day).

280   The Muskingum routing method is used to calculate the convergence process of the karst

281   underground river in this study, the equation is as follows:

282

283
$$
W = K[xI + (1-x)O] = KO'
\tag{4}
$$

284   Where O' is the water storage content, O is the outlet flow of the river reach, x is the

285   dimensionless proportion factor, I is the inflow discharge of the river reach, K is the slope of

286   the correlation curve of the water storage content and the discharge.

287   The finite difference method is used to calculate the water balance equation and the

288   Muskingum routing method:

289
$$\begin{cases} O_2 = C_0 I_2 + C_1 I_1 + C_2 O_1 \\ C_0 + C_1 + C_2 = 1 \end{cases} \tag{5}$$

290   where,

291
$$\begin{cases} C_0 = \dfrac{0.5\Delta t - Kx}{0.5\Delta t + K - Kx} \\ C_1 = \dfrac{0.5\Delta t + Kx}{0.5\Delta t + K - Kx} \\ C_2 = \dfrac{-0.5\Delta t + K - Kx}{0.5\Delta t + K - Kx} \end{cases} \tag{6}$$

292   If the parameter of the Muskingum routing method K and x could be determined for a

293   karst underground river reach, then the value of the C_0, C_1 and C_2 will be calculated by the

294   equation(6). When $\Delta t = 2Kx$, $C_0 = 0$, which means the karst flood forecasting lead time will

295   be $2Kx$, then the Muskingum routing method could be simplified as follows:

296
$$O_2 = C_1 I_1 + C_2 O_1 \tag{7}$$

297   One of the key problems of Muskingum routing method is to optimize the parameters -K

298   and x in the practical application. The least square method is used in this study:

299
$$\min \left\{ E = \sum_{j=1}^{n} \{W_0(j) - W_1(j) - C]^2 \right\} \tag{8}$$

300   Where E is the objective function between the observed water storage content and the

301   simulated one, which makes only require least squares approximation with regard to

302   functional value, $W_0(j)$ and $W_1(j)$ are the observed and simulated water storage content at j

303   period respectively, $W_1(j) = K[xI + (1-x)O]$, n is the total numbers of the observation

304   periods, C is the absolute value of the water storage content.

305   In order to simplify calculating, making $A = K_* x$, $B = K_* (1-x)$, then taking the partials with

306   respect to A, B, C respectively:

307
$$\begin{cases} \sum W_0 I = A \sum I^2 + B \sum (OI) + C \sum I^2 \\ \sum W_0 O = A \sum (OI) + B \sum O^2 + C \sum O \\ \sum W_0 I = A \sum I + B \sum O + Cn \end{cases} \tag{9}$$

308   Then the values of *A, B, C* could be calculated as follows:

309

$$
\begin{cases}
A = \dfrac{y_1}{y_2} - \dfrac{y_3}{y_2} \\[2mm]
B = \dfrac{y_1 z_2}{y_3 z_2} - \dfrac{y_2 z_1}{y_2 z_3} \\[2mm]
C = \sum \dfrac{W_0 - A\sum I - B\sum O}{n}
\end{cases}
\tag{10}
$$

310   Where,

311

$$
\begin{cases}
y_1 = \sum (W_0 I) - \dfrac{\sum W_0 \sum I}{n} \\[2mm]
y_2 = \sum I^2 - \dfrac{(\sum I)^2}{n} \\[2mm]
y_3 = \sum (IO) - \dfrac{\sum O \sum I}{n} \\[2mm]
z_1 = \sum (W_0 O) - \dfrac{\sum W_0 \sum O}{n} \\[2mm]
z_2 = \sum O^2 - \dfrac{(\sum O)^2}{n} \\[2mm]
z_3 = \sum IO - (\dfrac{\sum O \sum I}{n}) \\[2mm]
K = A + B \\[2mm]
x = \dfrac{K}{A}
\end{cases}
\tag{11}
$$

312   The parameters of the Muskingum routing method could be optimized through the above

313   equations. And after that, the convergence process of the karst underground river could be

314   calculated by the Muskingum routing method in Liuxihe model.

315   **3 Study area and data**

316   **3.1 Study area**

317   Liujiang Karst River Basin (LKRB) in southern China is selected as the study area in this

318   paper. It is the second largest tributary of Pearl River that covers three provinces including

319   Guizhou, Guangxi and Hunan province. LKRB is the most developed karst area of China with

320   a drainage area of 58270km^2 and a channel length of 1121 km. The carbonate rocks are

321   widely distributed in the southwest of the basin, and the areas account for 33% of the whole

322   watershed. LKRB is a typical karst-mountainous catchment with frequent flash flooding in

323   the past centuries .The peak forest-plain area is the main karst landform on the ground, while

324   the karst conduit and fissure are well-developed underground, also there are many

325   complicated underground rivers and springs with large flow (Li, 1996). The karst water-

326   bearing media is highly non-linear and heterogeneous, which makes it very difficult to

327   simulate and forecast the karst hydrological process.

328   LKRB is in the sub-tropical monsoon climate zone with an average annual precipitation of

329   1400mm to 1700mm, and the precipitation distribution is highly uneven at spatial and

330   temporal scale. The precipitation from April to September accounts for 75% to 80% of the

331   annual precipitation.

332   After studied the karst geomorphology of LKRB, Wil1iams (1987) believed that the

333   peak-cluster depression had developed into turreted peak-forest landforms after a long

334   evolutionary process, which is equivalent to the late prime of life, and going into the old age

335   of geomorphologic evolution as the tradition physiognomy theory by Davis (1912). The

336   allogenic water especially the Liujiang river is the main driving force for the development of

337   peak-forest landforms. Therefore, the peak-forest plains and valleys are often distributed in

338   contiguous areas near the main trunk stream of the Liujiang river. And the main karst

339   landform of LKRB is peak-forest plain, there are also some peak-cluster depressions and

340   peak-forest valleys. Figure 2. are the DEM and three-dimensional topographical map of

341   LKRB.

342

343   a. the DEM   b. three-dimensional topographical map

344   Figure 2. The DEM and three-dimensional topographical map of LKRB.

3.2 Rain gauges and the karst flood process

346   There are 68 rain gauges and 131 grid points of PERSIANN-CCS QPEs within LKRB

347   and five karst flood events from 2008 to 2013 has been collected respectively. There is a

348   flood event each year. The karst floods process in LKRB have typical characteristics: the

349   flood peak flows usually exceed 10,000m^3/s and expression of the multi-peaks flood process.

350   A flood process usually lasts about 10 days, and the shortest flood event duration is only

351   about 3 days, the longest is 25 days. The hourly precipitation data of rain gauges are collected

352   in this study to compare with the results of PERSIANN-CCS QPEs. The rain gauges, grid

353   points of PERSIANN-CCS QPEs and the Liuzhou river gauge that closes to the outlet of

354   LKRB are shown in Figure 3.

355   Figure 3. Sketch map of Liujiang River Basin (LKRB)

3.3 Property data

356
357   Catchment property data for distributed hydrological model mainly include DEM, land
358   use and soil types. These data are downloaded from an open access databases. The DEM is
359   downloaded from the shuttle radar topography mission database at http://srtm.csi.cgiar.org
360   (Falorni et al., 2005, Sharma et al., 2014). The downloaded DEM has an initial spatial
361   resolution of 90m*90m, and after many model resolution tests, the most appropriate
362   resolution has been confirmed as 200m*200m for Liuxihe model in LKRB. So the spatial
363   resolution of the initial DEM is rescaled to 200m*200m in this study, which is a high
364   resolution for Liuxihe model in LKRB. The DEM is shown in Figure 2(a).The land use type
365   is downloaded from http: //landcover.usgs.gov (Loveland et al., 1991, 2000), and the soil type
366   is downloaded from http://www.isric.org. The initial spatial resolutions of the land use type
367   and soil type are 1000m*1000m. Both of them need to be rescaled to 200m*200m in this
368   study. Figure 4 (a) is land use types and (b) is soil types.

369   Figure 4. The property data for Liuxihe model in LKRB

4 PERSIANN-CCS QPEs and its post-processed results

371   4.1 Precipitation estimation results

372   The QPEs product of PERSIANN-CCS has been generated precipitation result for LKRB
373   in this study. There are 131 grid points of PERSIANN-CCS QPEs within LKRB , which are
374   representative and can cover the whole watershed completely (as shown in Figure 3).The
375   precipitation estimation results by PERSIANN-CCS QPEs has been downscaled as the same
376   temporal-spatial resolution as Liuxihe model, the spatial resolution is 200m*200m and the
377   time interval is 1 hour. The QPEs products of PERSIANN-CCS in 2008,2009,2011,2012 and
378   2013 are produced respectively, means there are five rainfall events are corresponding to the
379   five karst flood processes. Figure 5-9 is the average precipitation pattern comparisons of two
380   precipitation products in the five years, and (a) is the average precipitation of rain gauges, (b)
381   is the average precipitation of PERSIANN-CCS QPEs.

382   Figure 5. Precipitation pattern comparison of two precipitation products(2008), (a) is the average
383   precipitation of rain gauges, (b) is the average precipitation of PERSIANN-CCS QPEs.

384   Figure 6. Precipitation pattern comparison of two precipitation products(2009), (a) is the average
385   precipitation of rain gauges, (b) is the average precipitation of PERSIANN-CCS QPEs.

386   Figure 7. Precipitation pattern comparison of two precipitation products(2011), (a) is the average
387   precipitation of rain gauges, (b) is the average precipitation of PERSIANN-CCS QPEs.

388   Figure 8. Precipitation pattern comparison of two precipitation products(2012), (a) is the average
389   precipitation of rain gauges, (b) is the average precipitation of PERSIANN-CCS QPEs.

390   Figure 9. Precipitation pattern comparison of two precipitation products(2013), (a) is the average
391   precipitation of rain gauges, (b) is the average precipitation of PERSIANN-CCS QPEs.

392   According to the results of Figure 5-9, it appears that the temporal average precipitation

393   pattern of both products are quite similar, especially in the rainfall distribution, while there

394   are some difference in the quantitative value. The results of PERSIANN-CCS QPEs are

395   smaller than that of the rain gauge, which means there is a relative error exists between the

396   two products.

397   4.2 Evaluation of PERSIANN-CCS QPEs

398   In order to quantitatively evaluate the results of PERSIANN-CCS QPEs, the

399   precipitation by PERSIANN-CCS QPEs and rain gauge are compared in this study. The

400   rainfall distribution of both products are shown in Figs. 5–9.To make further comparison, the

401   average precipitation of the five karst flood events are calculated in Table 1.

402   Table1. Precipitation pattern comparison of two precipitation products

403   According to the results of Table 1, it could be found that there are obvious relative

404   errors between the two precipitation products. The average precipitations of PERSIANN-CCS

405   QPEs are smaller than that of the rain gauge. For the five karst flood events from 2008 to

406   2013, the relative errors between two products are -16%,-25%,-14%,-21% and -23%

407   respectively. The average relative error is -20% and the maximum error is -25%, which

408   means these relative errors could not be ignored. So the precipitation results by PERSIANN

409   QPEs must to be revised effectively, the precipitation data observed by rain gauge are used to

410   revise the results of PERSIANN QPEs in this study.

411   4.3 The post-processed PERSIANN-CCS QPEs

412   In order to make the results of PERSIANN QPEs more credible and receivable, the

413   precipitation results by PERSIANN QPEs are revised with the observed precipitation by rain

414   gauge. Firstly, finding the grid points of PERSIANN-CCS QPEs that are adjacent the rain

415   gauges (as shown in Figure 3). And there are 23 grid points in LKRB. Secondly, calculating

416   their average precipitation of PERSIANN-CCS QPEs and rain gauges, and taking the average

417   precipitation of rain gauges as the true precipitation. Thirdly, revising the results of

418   PERSIANN QPEs with the average precipitation observed by rain gauges.The procedure is

419   summarized as follows.

420   1). Calculating the average precipitation of these 23 grid points based on PERSIANN-CCS

421   QPEs with the following equation.

$$\bar{P}_{PERSIANN-CCS} = \frac{\sum_{i=1}^{N} P_i F_i}{N} \qquad (1)$$

423 Where, $\bar{P}_{PERSIANN-CCS}$ is the average precipitation of these 23 grid points by PERSIANN-CCS

424 QPEs; P_i is the precipitation based on PERSIANN-CCS QPEs on the i grid point; F_i is the

425 catchment area of the i grid point; N is the number of the grid points.

426 2). Calculating the average precipitation of these 23 rain gauges.

$$\bar{P}_2 = \frac{\sum_{j=1}^{M} P_j}{M} \qquad (2)$$

428 Where, $\bar{P}_2$ is the average precipitation observed by these 23 rain gauges; P_j is the

429 precipitation by the j rain gauge; M is the number of rain gauges.

430 3). The precipitations observed by the adjacent rain gauges are used to revise the results of
431 PERSIANN-CCS QPEs with the following equation.

$$P_i' = P_i \frac{\bar{P}_2}{\bar{P}_{PERSIANN-CCS}} \qquad (3)$$

433 Where, P_i' is the value of precipitation based on PERSIANN-CCS QPEs after revised on the i

434 grid point; $\bar{P}_2 / \bar{P}_{PERSIANN-CCS}$ is the revise factor.

435 4). The precipitation results based on PERSIANN-CCS QPEs after revised will be as input
436 data for Liuxihe model to test its feasibility through the floods simulation.

437   From the above procedure of the post-processed PERSIANN-CCS QPEs, it could be

438 found that the revise factor- $\bar{P}_2 / \bar{P}_{PERSIANN-CCS}$ is a key to make the results of PERSIANN-

439 CCS QPEs much closer to the observed precipitation by rain gauges, means the systematic

440 errors of the PERSIANN-CCS QPEs could be corrected effectively. So the post-processed

441 method in this paper is a feasible and necessary. And it could greatly improve the accuracy of

442 the coupling model in karst flood simulation and forecasting. Furthermore, the revise factor

443 could be preserved as an empirical value for the future flood forecasting in LKRB.

5 Model set up

444

445 5.1hydrological model setup

446   The method combining DEM with stream network leads to a more accurate drainage

447 network from surface runoff modelling (Li and Tao,2000), especially in karst area. In this

448 study, according to the high resolution of 200m*200m for Liuxihe model in LKRB, the whole

449 studied area is divided into 1,469,900 grid cells named the karst sub-basins by using the DEM.

450 The grid cells include 1,463,204 hill slope cells and 6,696 river cells. Then the karst sub-

451 basins will be divided into many karst hydrology respond units (KHRUs) further, the KHRU

452 is as shown in Figure 1. The river system are divide into three-order by Strahler method

453 (Strahler,1957) as shown in Figure 3.

454   Because of the sinkholes and karst depressions in karst watershed, as well as the

455 systematic error of the DEM itself, there are many pits including the true and false pits in

456 LKRB. Among them the true pits are the karst depressions and sinkholes, they usually have a

457 certain scale with elevation difference. While the false pits are just few points with low

458 elevation, which is due to the systematic errors of the DEM. So the true and false pits should

459 be distinguished reliably before using DEM data to divide into the karst sub-basins. Firstly,

460 finding out all the pits with low elevation, and connect them into a plane, then distinguish the

461 true pits from the false ones according to the on-site topographic survey. Finally,keeping the

462 true pits like the sinkholes and karst depressions unchanged but filling the false pits in the

463 model.

464   The karst hydrology respond unit (KHRU) is introduced in this study to reasonably

465 describe the spatial variability of the karst water-bearing media (as shown in Figure1). The

466 spatial characteristic of every KHRU has definite physical meaning. So the calculation of the

467 evapotranspiration, rainfall-runoff and parameter optimization on the KHRU is also

468 physically based, which could truly reflect the differences of the underlying surface. After the

469 division of the karst sub-basins and the KHRUs, the post-processed PERSIANN-CCS QPEs

470 results will be as the input data for Liuxihe model to simulate and forecast the karst flood

471 process. The performance of the coupling model could be improved reliably in this way.

472   5.2 Parameter optimization of coupling model

473   There are many parameters need to be optimized for a distributed hydrological model, as

474   shown in Table.2, among them the parameters of soil water properties, the epikarst zone and

475   the underground river are the most sensitive parameters for the coupling model in this study.

476   The parameters of the epikarst zone are the most complicated due to the anisotropy of the

477   karst water-bearing media, which makes it hard to measure and calculate the hydraulic

478   characteristics. According to the field survey, the epikarst zone is mainly developed on the

479   hard surface of pure carbonate rock, especially on the Paleozoic limestone. The thickness and

480   characteristics of the epikarst zone are different due to the different climate, topography and

481   landforms. And the thickness of the epikarst zone is about 10 meters in the study area- LKRB.

482   The parameters of the coupling model are listed inTable 2.

                            Table 2. The parameters of the coupling model

484   The parameters of the Soil type like the saturated water content and field capacity are

485   calculated through a software tool by the research result of Saxton (Saxton et al.,1986) .The

486   statistical relation between the soil texture and the soil water could be queried easily in the

487   software tool. And it has been effectively proved by many experiments (Servat and

488   Sakho,1995), the calculated value of this method has a good fitting relation with the measured

489   value.

490   Liuxihe Model has been deployed on a supercomputer system with parallel computation

491   technology (Chen et al., 2011) .An improved PSO algorithm (Chen et al., 2017)is employed

492   to optimize the parameters of the coupling model in this study. And the flood process for

493   parameter optimization is the Flood 2009060908. The results of parameters optimization are

494   shown in Figure 10, among them, (a) is the objective function evolution result, (b) is the

495   parameters evolution result, and (c) is the simulated flood process by using the optimized

496   model parameters.

497   Figure 10. Parameter optimization results with the improved PSO algorithm

498   From the results of Figure 10(c), it could be found that the coupling model with initial

499   model parameter values does not simulate the observed karst flood process satisfactorily, and

500   compared with that, the parameters optimization with the improved PSO algorithm could

501   largely improve the coupling model's performance. The simulated flood process is very close

502   to the observed value.

503   In order to test the parameters optimization effect with different precipitation sources,

504   both the precipitation of the rain gauge and PERSIANN CCS QPEs are used to optimize the

505   parameters of the coupling model. To compare with that, the simulated flood process of the

506   coupling model with the same parameter as rain gauges and re-optimized parameter with the

507   post-processed PERSIANN CCS QPEs are also drawn in Figure 10(c).

508   From the results of Figure 10(c), it could be found that the coupling model with the re-

509   optimized parameters by the post-processed PERSIANN CCS QPEs has a better flood

510   simulation effect than that of with the same parameter as rain gauges precipitation, which

511   means re-optimized parameters with the post-processed PERSIANN CCS QPEs for the

512   coupling model is necessary.

513   5.3 Model validation

514   The karst flood process for parameter optimization is the Flood 2009060908 in this

515   study. Other four floods including Flood 200806090200, Flood 201106010900, Flood

516   201206022000 and Flood 201306011400 are used to validate the performance of the coupling

517   model. The flood simulation results are drawn in Figure 11.

518   Figure 11. The flood simulation results of the coupling model with two precipitation products

519   From the result of Figure 11, it could be seen that the simulated karst flood discharges

520   with the precipitation of rain gauge are the best. And the simulated values are the closest to

521   the measured values, especially the simulated flood peaks are satisfactory, which is the most

522   concerned factor in real-time flood forecasting. The average values of six evaluation indices,

523   including the Nash–Sutcliffe coefficient (C), correlation coefficient (R), process relative error

524   (P), peak flow relative error (E) ,water balance coefficient (W), and peak flow time error (T)

525   are 0.86, 0.86, 18%, 4% , 0.91, and -7 hours respectively (as shown in Table 3). This means

526   parameters optimization with the improved PSO algorithm in this study is effective. From

527   Figure 11, it may be seen that the karst flood simulation results with the initial PERSIANN

528   CCS QPEs are not so satisfactory, and the performance of the model are worse than that of

529   the rain gauge precipitation. While the flood simulation results of the coupling model with the

530   post-processed PERSIANN CCS QPEs are much better, also the evaluation indices of the

531   flood simulation have been largely improved.

532   **6 Results and discussions**

533   In order to test the effects of the flood simulation of the coupling model with the post-

534   processed PERSIANN-CCS QPEs as well as the coupling model with different parameters.

535   Two test methods are used in this paper:

536   1)   Keeping the coupling model parameters unchanged, means the coupling model takes the

537   same parameters as the precipitation of the rain gauge. The flood simulation effects with

538   the initial PERSIANN-CCS QPEs and the post-processed ones could be compared in this

539   way.

540   2) Re-optimizing the coupling model parameters, means the post-processed PERSIANN-
541   CCS QPEs are used to re-optimize the coupling model parameters again to test its
542   necessity.

543   6.1 Results of flood simulation with the post-processed PERSIANN-CCS QPEs

544   After the correction, the post-processed PERSIANN-CCS QPEs precipitation has
545   become much closer to the observed precipitation of rain gauge. In order to analyze the
546   effects of flood simulation with the post-processed PERSIANN-CCS QPEs, five karst flood
547   events including Flood 200806090200, 200906090800, 201106010900, 201206022000 and
548   201306011400 are used in this paper, and the flood simulation results with different
549   precipitation sources including the rain gauges precipitation, the PERSIANN-CCS QPEs and
550   its post-processed results are compared in Figure 11. In this simulation, keeping the coupling
551   model parameters unchanged, means the coupling model with the same parameters as the rain
552   gauges precipitation, not the re-optimized parameters with the post-processed PERSIANN-
553   CCS QPEs results. The flood simulation results are shown in Figure 11.

554   From Figure 11, it could be seen that the simulated flood discharges with the
555   precipitation of rain gauge are better than that of the PERSIANN-CCS QPEs. And the
556   simulated peak flows with the PERSIANN-CCS QPEs are lower than the observed ones.
557   However, the flood simulation effects with the post-processed PERSIANN-CCS QPEs make
558   a great progress, the simulated flood processes fit the observation values reasonably, and
559   simulated peak flows are much closer to the observation ones. It implies that the flood
560   forecasting capability has been largely improved by the post-processed method of the
561   PERSIANN-CCS QPEs.

562   To further compare the flood simulation results, six evaluation indices are calculated and
563   listed in Table 3. It has been found that all the six evaluation indices of rain gauges are better
564   than that of PERSIANN-CCS QPEs. And the indices of QPEs have been improved a lot with
565   the post processed QPEs. The average value of Nash–Sutcliffe coefficient has a 7% increase,
566   the correlation coefficient has a 8% increase, process relative error has a 6% decrease, peak
567   flow relative error has a 14% decrease, the water balance coefficient has a 5% increase, and
568   peak flow time error has 7 hours decrease, respectively. Among them, the peak flow relative
569   error has the biggest improvement. It is obvious that the evaluation indices are improved
570   substantially with the post-processed QPEs. So it implies the post-processed method for
571   PERSIANN-CCS QPEs in this paper is feasible and effective. And coupling the post-
572   processed PERSIANN-CCS QPEs with Liuxihe model has the potential to improve the model
573   performance in flood simulation and forecasting in LKRB.

6.2 Effects comparison of different model parameters

The performance of the coupling model makes a big difference with different parameters. There are two different sets of model parameter values in this study, one is the parameters with the precipitation of rain gauge, and the other is the parameters with the post-processed PERSIANN-CCS QPEs. The post-processed PERSIANN-CCS QPEs are used to re-optimize the coupling model parameters again to test its necessity. And the flood simulation results with two different sets of model parameters are shown in Figure 12.

Figure 12. Coupled flood simulation results with the same parameter as the rain gauge precipitation and re-optimized parameter with the post-processed PERSIANN-CCS QPEs

From the above results in Figure 12, it has been found that the simulated flood results with re-optimized parameters by the post-processed PERSIANN-CCS QPEs are much better than that of with the same parameter as rain gauge precipitation. The simulated flood discharge processes, especially the peak flows with the re-optimized parameter are closer to the observation values. To further compare the flood simulation results, six evaluation indices are calculated in Table 4, the average value of Nash–Sutcliffe coefficient has a 7% increase, the correlation coefficient has a 6% increase, process relative error has a 2% decrease, peak flow relative error has a 4% decrease, the water balance coefficient has a 2% increase, and peak flow time error has 18 hours decrease, respectively. What is more, comparing with the simulated flood results of the initial PERSIANN-CCS QPEs in Table 3, the average value of Nash–Sutcliffe coefficient has a 14% increase, the correlation coefficient has a 14% increase, process relative error has a 8% decrease, peak flow relative error has a 18% decrease, the water balance coefficient has a 7% increase, and peak flow time error has 25 hours decrease, respectively (as shown in Table 3 and Table 4). So it implies the re-optimized parameters with the post-processed PERSIANN-CCS QPEs for the coupling model is necessary and effective, which makes a better performance for the coupling model in karst flood simulation and forecasting.

6.3 Peak flow time error analysis

It is very important to accurately determine the flood peak flow time in karst area, which could offer enough response times for evacuation safely and rapidly before the flood disaster appears. From the above results in Figure 11, 12 and Table 3, 4, it has been found that all flood simulations have significant peak flow time errors, and all of them are negative, means the simulated flood peaks appeared earlier than the observed values. Among them the average peak flow time error with the precipitation of rain gauge is -7 hours, and that is -32 hours with the precipitation of the initial PERSIANN-CCS QPEs. It is an obvious error and could not be ignored in flood forecasting. While the average peak flow time error of the coupling model

610   with the post-processed PERSIANN-CCS QPEs precipitation and re-optimized parameters is

611   also -7 hours. It makes a great difference. It has been found that both the average peak flow

612   time errors of Liuxihe model with the precipitation of rain gauge and the coupling model with

613   the precipitation of the post-processed PERSIANN-CCS QPEs and re-optimized parameters

614   are -7 hours (as shown in Table 4). So it implies the peak flow time error is -7 hours for the

615   coupling model in LKRB, means the actual time of the flood peak may be 7 hours later,

616   which is very important in flood forecasting and equivalent to a 7 hours long lead time for

617   evacuation safely.

618   There are two reasons for the peak flow time errors. One is the systematic error of the

619   coupling model itself. And that could be reduced by improving the model structure and

620   function as well as the reliable precipitation by PERSIANN-CCS QPEs and parameters

621   optimization. The other is due to the karst development laws and the characteristics of karst

622   water-bearing media, which can regulate the rainfall process during floods. The karst

623   depressions and other karst negative landforms in the upstream regions can hold back and

624   store some large floods. What is more, the karst fissures can also slow down the floods rate.

625   These factors can play a crucial role in natural flood detention and peak clipping. So the

626   response times of flood peak flow to rainfall increased, and the observed flood peak times

627   lagged behind. In comparison, the simulated flood peak flows appear ahead of time.

628   The rainfall process from the sky to the ground and finally converge to the outlet of the

629   basin has passed through the surface karst zone, the karst conduit and fissure as well as the

630   underground river. And the karst development laws and the characteristics of karst water-

631   bearing media have obvious influence on the rainfall-runoff process during the whole

632   hydrological process, which makes the response time of flood peak flow to rainfall increases,

633   and the simulated flood peak flow by the coupling model appears earlier. It implies there is a

634   lead time for evacuation safely in flood forecasting.

635   The flood peak flow time has a very close relationship with the floods rate, and the

636   floods rate is very important to determine the key factors of the karst conduit, the

637   underground river and other hydrogeological parameters. The sensitive parameters in this

638   paper such as the underground river parameters (as shown in Table 2) could be estimate from

639   the floods rate to build the coupling model in karst areas. According to the survey data and

640   tracing test in the study area – LKRB, the flow rate of floods is about 8.64-17.28km/d in dry

641   season; that is 17.28-43.2 km/d in the normal season and is 43.2-129.6 km/d in flood period.

642   The extreme flow rate can reach 172.8km/d, means the karst conduit is very developed in

643   LKRB.

7 Conclusion

645   There is no reliable precipitation data of rain gauges in many karst river basins. How to

646   obtain the reasonable rainfall data for the hydrological model in flood forecasting is especially

647 important. In this study, the PERSIANN-CCS QPEs could offer effective precipitation results

648 for the study area. And after the correction, the post-processed PERSIANN-CCS QPEs coupled

649 with a distributed hydrological model-Liuxihe model is proposed in karst flood simulation

650 and forecasting in LKRB. The purpose is not only to simulate the flood process well, but also

651 to find out the key factor how the karst hydrological process responds to the rainfall process

652 in the coupling model. The coupling model employed in this paper has a good performance in

653 flood events simulation, which can offer a reasonable theoretical guidance for flood

654 forecasting, control and disaster reduction in karst river basins like LKRB. Based on the study

655 results, the following conclusions could be drawn:

656 1). The quantitative precipitation estimates produced by the PERSIANN-CCS QPEs are quite

657 similar to the observed precipitation by rain gauges, especially in the rainfall distribution. But

658 the PERSIANN-CCS QPEs underestimates the precipitation value. The average precipitation

659 is 0.29 for rain gauges and 0.23 for PERSIANN-CCS QPEs.

660 2). The average relative error is 20% between the two precipitation products. And this relative

661 error could be reduced reasonably by the post-processed method in this paper. The average

662 values of the six evaluation indices including the Nash–Sutcliffe coefficient (C), correlation

663 coefficient (R), process relative error (P), peak flow relative error (E), water balance

664 coefficient (W), and peak flow time error (T) with the initial PERSIANN-CCS QPEs are

665 0.66,0.69,0.28, 24%, 0.81 and -32 hours, respectively, while those with the post-processed

666 QPEs are 0.73, 0.77, 0.22, 10%,0.86 and -25 hours, respectively. It means the method used in

667 this study for QPEs post-processed is effective, and could improve the effect of the

668 PERSIANN-CCS QPEs capability.

669 3). The coupling model parameters should be re-optimized using the post-processed

670 PERSIANN-CCS QPEs. Because it has a better performance in the flood simulation than the

671 same model parameters as rain gauges. The average value of Nash–Sutcliffe coefficient (C),

672 correlation coefficient (R), process relative error (P), peak flow relative error (E) ,water

673 balance coefficient (W), and peak flow time error (T) with the same model parameters as rain

674 gauge are 0.73, 0.77, 0.22, 10%,0.86 and -25 hours, respectively, but those with the re-

675 optimized model parameters are 0.80, 0.83, 0.20, 6%,0.88 and -7 hours, respectively. It

676 improves the model performance significantly.

677 4). The simulated karst floods process based on the precipitation observed by rain gauges is

678 the best. And the flood simulation results by PERSIANN-CCS QPEs after post-processed and

679 re-optimized model parameters could make the coupling model performance much better. The

680 average value of Nash–Sutcliffe coefficient has a 14% increase, the correlation coefficient has

681 a 14% increase, process relative error has a 8% decrease, peak flow relative error has a 18%

682 decrease, the water balance coefficient has a 7% increase, and peak flow time error has 25

683 hours decrease, respectively. Among them, the peak flow relative error and peak flow time

684 error have the biggest improvement, which are the greatest concerned factors in a flood

685 forecasting in karst river basins.

Data availability

687 The rain gauge precipitation and river flow discharge data are provided by the Bureau of Hydrology,

688 Pearl River Water Resources Commission, China, exclusively used for this study. The PERSIANN

689 QPEs data are provided by Center for Hydrometeorology and Remote Sensing, Department of Civil

690 and Environmental Engineering, University of California, Irvine. The Liuxihe model used in this study

691 is provided by Yangbo Chen, Department of Water Resources and Environment, Sun Yat-sen

692 University, Guangzhou , China

Competing interests.

694 The authors declare that they have no conflict of interest.

695 **Acknowledgements.** This Study is supported by the Open Project Program of Chongqing Key

696 Laboratory of Karst Environment (Grant No. Cqk201801). The Chongqing Municipal Science and

697 Technology Commission Fellowship Fund (No. cstc2016jcyjys0003), and the National key research

698 and development program of China (2016YFC0502306)

699 Edited by: Ji Li

700

701 **Figures**
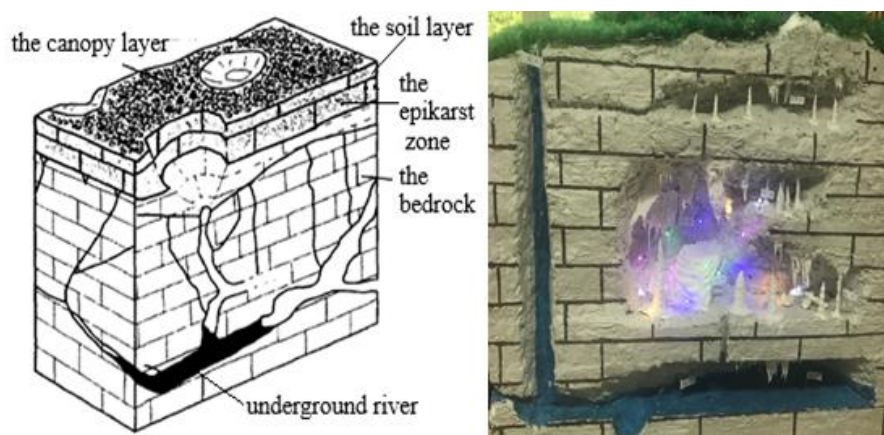
702

703   a. The structure of the KHRU(Ren, Q.W.,2006)   b. The photograph of the three-
704   dimensional space structure of the KHRU

705   Figure 1. Sketch map of the KHRU

706

707

708

709

710

711

712

713

714

715
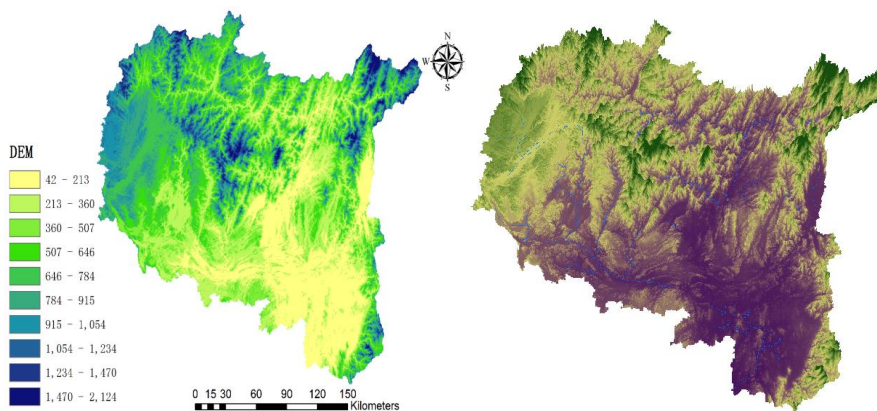
716   a. The DEM map   b. Three-dimensional topographical map

717   Figure 2. The DEM and three-dimensional topographical map of LKRB.

718
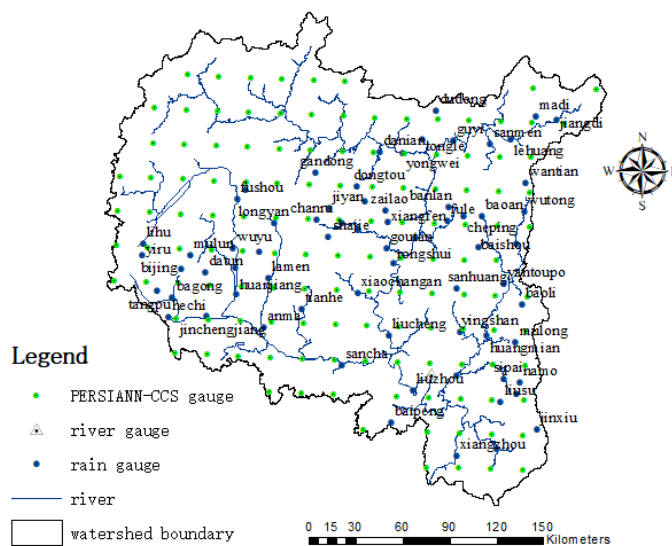
719

720   Figure 3. Sketch map of Liujiang River Basin (LKRB)

721

722

723

724

725

726

727

728   (a) Land use   (b) Soil type
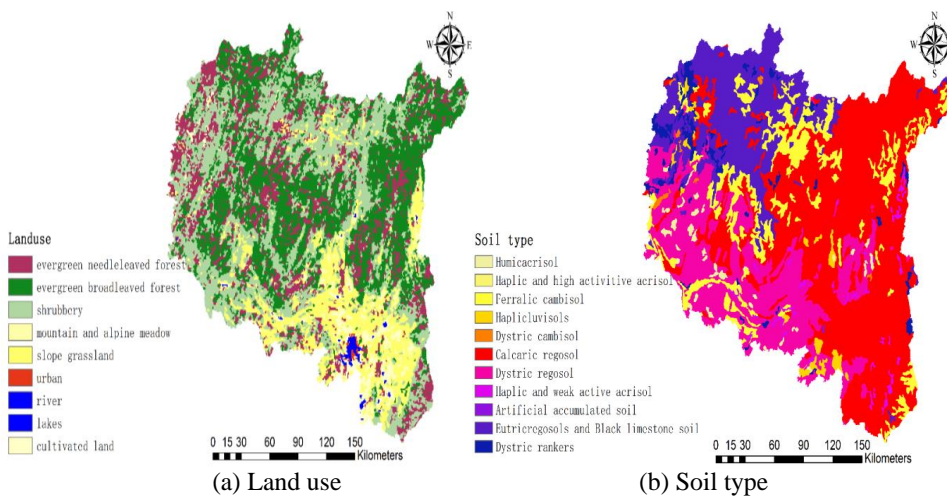
729   Figure 4. The property data for Liuxihe model in LKRB

730

731

732

733
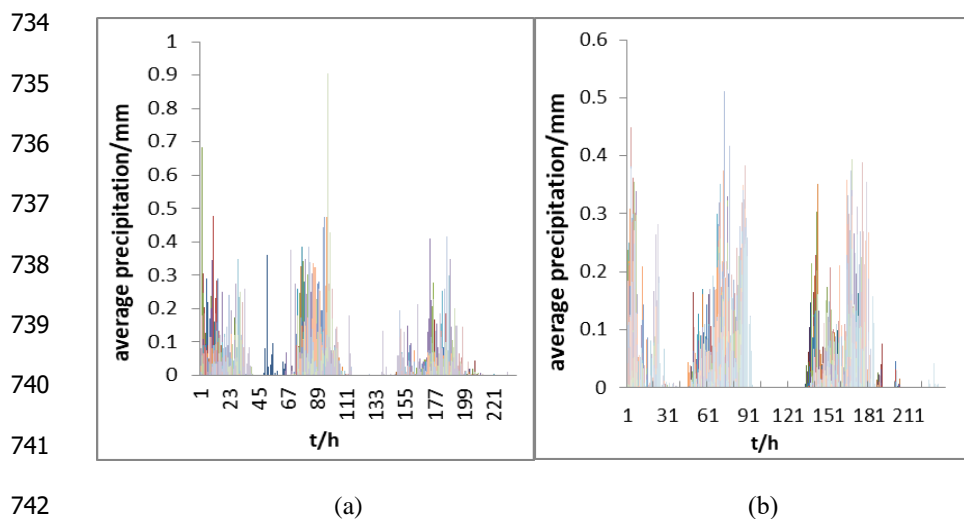
(a)   (b)

Figure 5. Precipitation pattern comparison of two precipitation products(2008), (a) is
the average precipitation of rain gauges, (b) is the average precipitation of
PERSIANN-CCS QPEs.

(a)   (b)
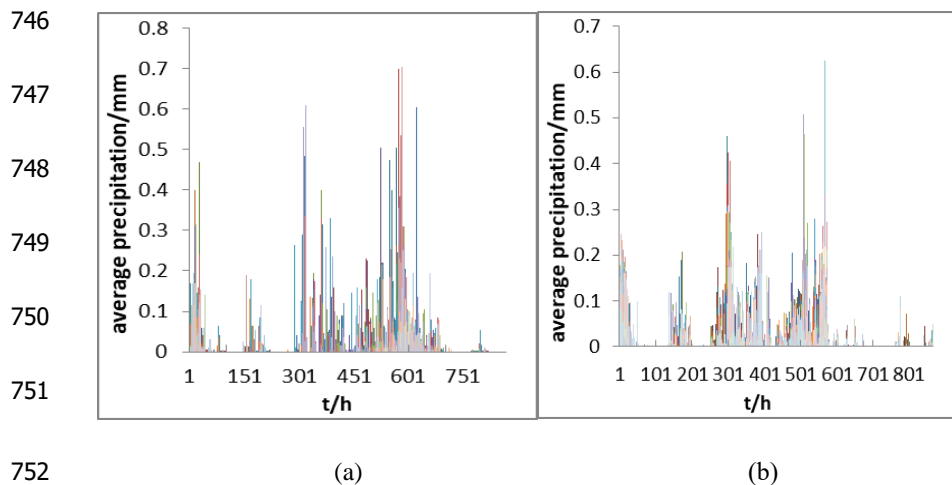
Figure 6. Precipitation pattern comparison of two precipitation products(2009), (a) is
the average precipitation of rain gauges, (b) is the average precipitation of
PERSIANN-CCS QPEs.

759
760
761
762
763
764

765   (a)   (b)
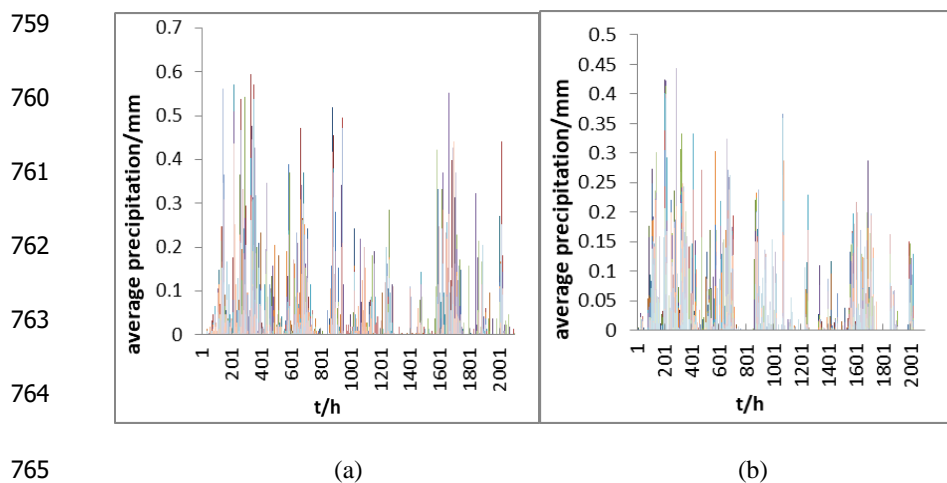
766   Figure 7. Precipitation pattern comparison of two precipitation products(2011), (a) is
767   the average precipitation of rain gauges, (b) is the average precipitation of
768   PERSIANN-CCS QPEs.

769
770
771
772
773
774
775
776
777

778   (a)   (b)
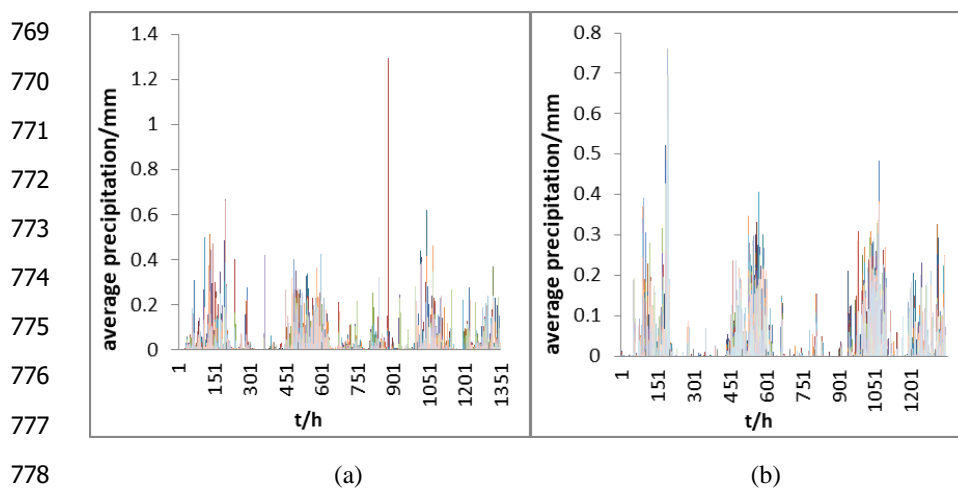
779   Figure 8. Precipitation pattern comparison of two precipitation products(2012), (a) is
780   the average precipitation of rain gauges, (b) is the average precipitation of
781   PERSIANN-CCS QPEs.

782
783
784
785
786
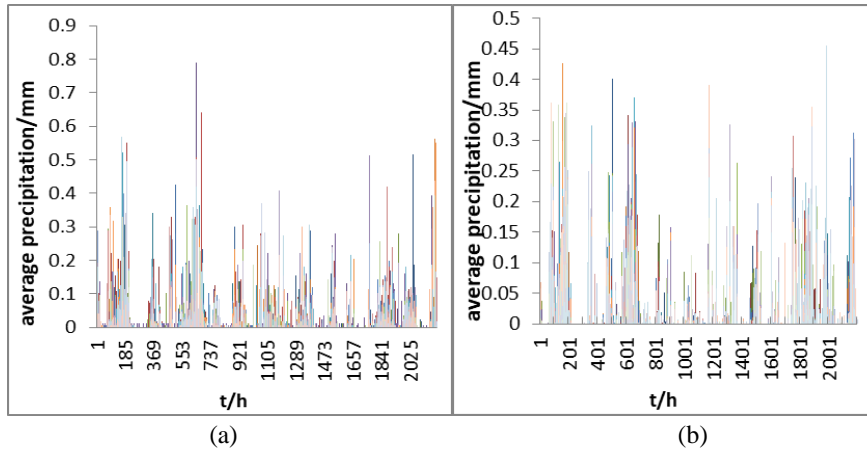
Figure 9. Precipitation pattern comparison of two precipitation products(2013), (a) is the average precipitation of rain gauges, (b) is the average precipitation of PERSIANN-CCS QPEs.
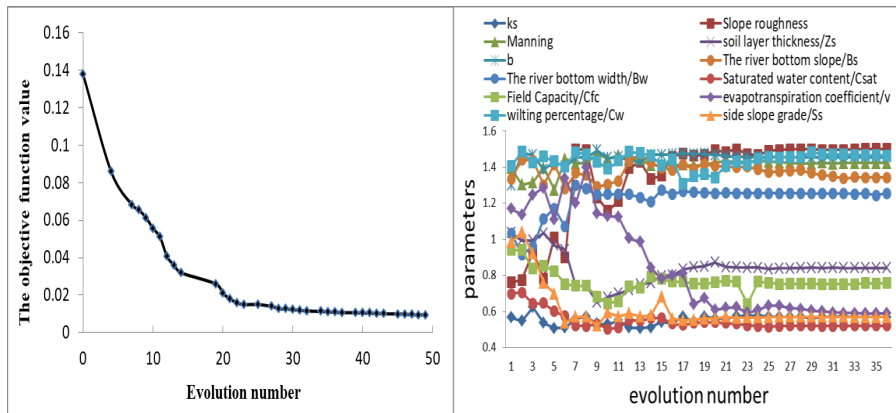
(a) The objective function evolution result   (b) The parameters evolution result
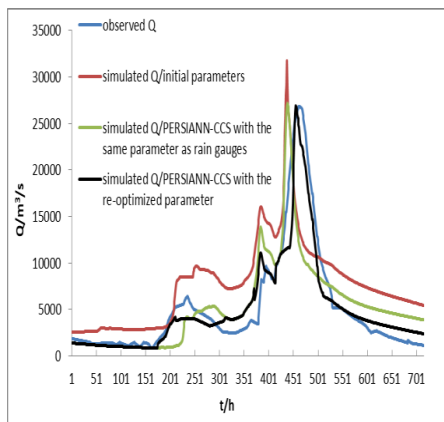
817 (c) The simulated flood process by using the optimized model parameters
818   Figure 10. Parameter optimization results with the improved PSO algorithm
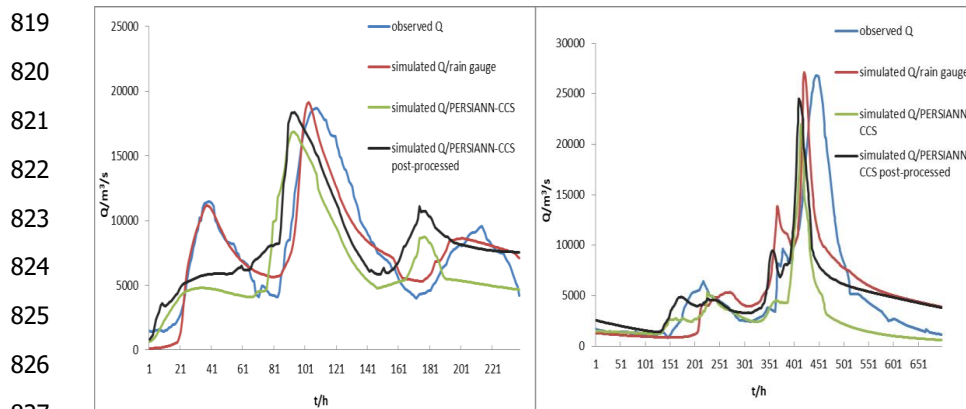
828   (a)flood event 200806090200   (b) flood event 200906090800
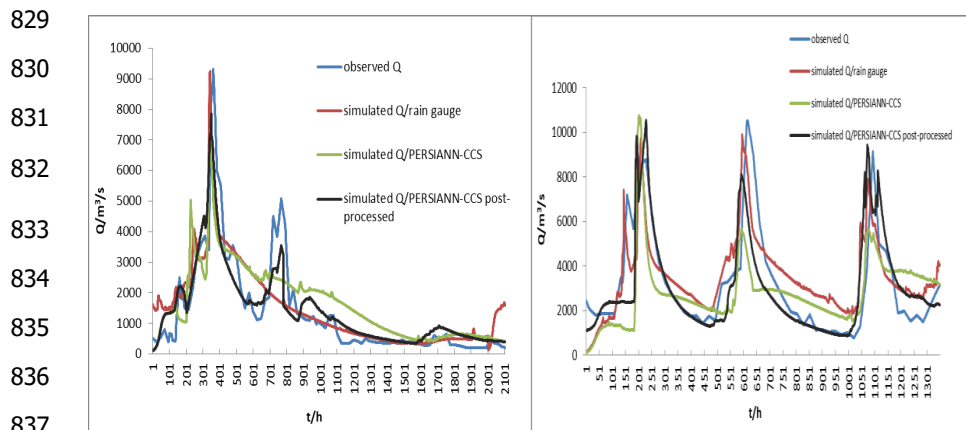
838   (c) flood event 201106010900   (d) flood event 201206022000
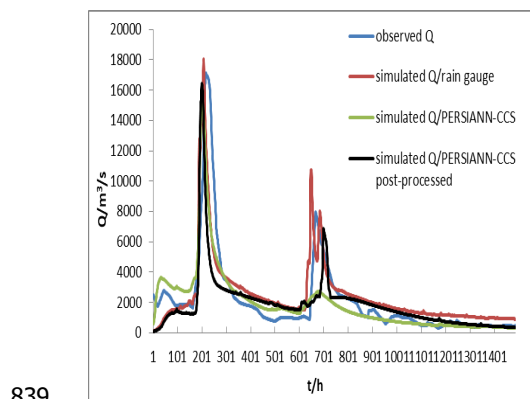
840   (e) flood event 201306011400

841  Figure 11. The flood simulation results of the coupling model with two precipitation

842          products

843

844

845

846

847

848

849

850

851

852
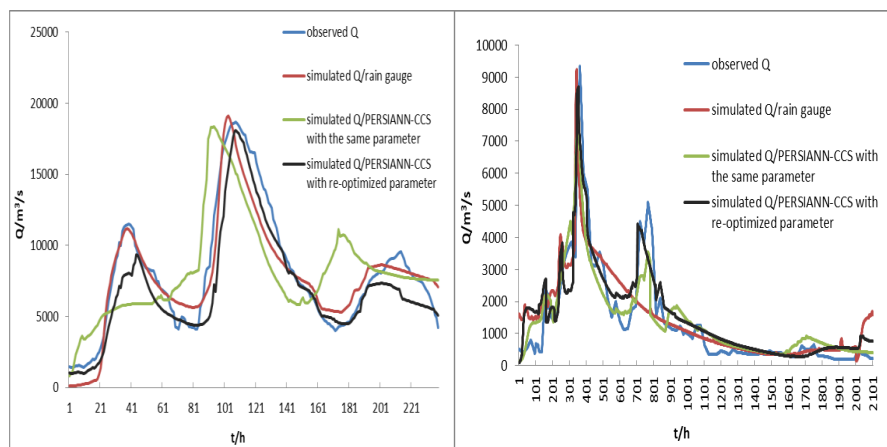
853   (a)flood event 200806090200   (b) flood event 201106010900

854

855

856

857

858

859

860

861

862
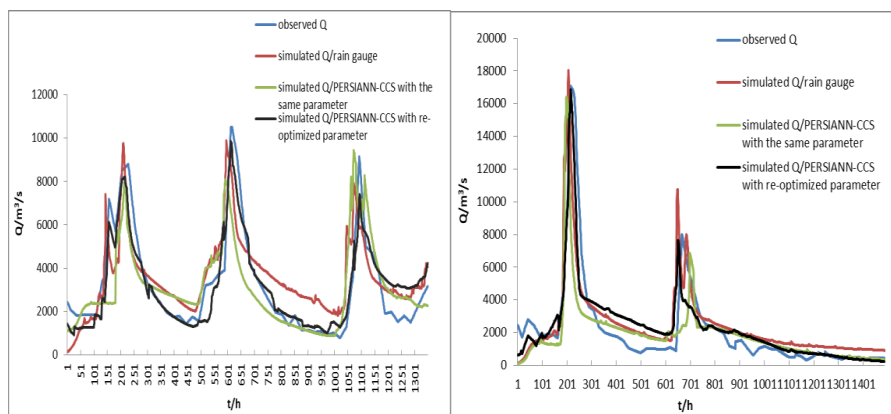
863   (c) flood event 201206022000   (d) flood event 201306011400

864   Figure 12. Coupled flood simulation results with the same parameter as the rain

865 gauge precipitation and re-optimized parameter with the post-processed PERSIANN-

866         CCS QPEs

867

868   **Tables**

869   Table 1. Precipitation pattern comparison of two precipitation products

flood	type	average precipitation(mm)	relative bias %
200806090200	rain gauge	0.37	
	PERSIANN-CCS QPEs	0.31	-16
200906090800	rain gauge	0.24	
	PERSIANN-CCS QPEs	0.18	-25
201106010900	rain gauge	0.22	
	PERSIANN-CCS QPEs	0.19	-14
201206022000	rain gauge	0.38	
	PERSIANN-CCS QPEs	0.30	-21
201306011400	rain gauge	0.22	
	PERSIANN-CCS QPEs	0.17	-23
average value	rain gauge	0.29	
	PERSIANN-CCS QPEs	0.23	-20

870

871   Table 2. The parameters of the coupling model

Parameters types	Name	Variable name	Physical property	Sensitivity	Adjustability
Evapotranspiration	Potential evaporation	E_p	Meteorology	insensitive	adjustable
	Evaporation coefficient	λ	Vegetation type	sensitive	adjustable
	Wilting percentage	C_{wl}	Vegetation type	insensitive	adjustable
The epikarst zone	Thickness	h	Soil type& Karst rock property	sensitive	unadjustable
	Saturated water content	θ_{sat}	Soil type	highly sensitive	adjustable
	Saturation permeability coefficient	θ_s	Soil type	highly sensitive	adjustable
	Wide crack volume ratio	V	Karst rock property	highly sensitive	adjustable
	Field capacity	θ_{fc}	Soil type	sensitive	adjustable
Rainfall-runoff	Soil layer thickness	z	Soil type	sensitive	adjustable
	Saturated hydraulic conductivity	K_s	Soil type	highly sensitive	adjustable
	Soil coefficient	b	Soil type	sensitive	adjustable
	Flow direction	F_d	Landform	highly sensitive	unadjustable

	Slope	S0	Landform	highly sensitive	unadjustable
	Bottom slope	Sp	Landform	sensitive	adjustable
	Bottom width	Sw	Landform	sensitive	adjustable
	Slope roughness	n	Landform &Vegetation type	sensitive	adjustable
	Channel roughness	n1	Landform &Vegetation type	sensitive	adjustable
The undergrou nd river	Depletion coefficient	ω	Landform &Soil type	sensitive	adjustable
	Muskingum routing method / The slope of the water storage content and flow curve	K	Landform	highly sensitive	adjustable
	Muskingum routing method/the proportion of the flow	χ	Landform	highly sensitive	adjustable

872   Table 3. Evaluation indices of simulated flood events with the post-processed
873   PERSIANN-CCS QPEs

flood	type	Nash-Sutcliffe coefficient/C	Correlation coefficient/ R	Process relative error/P %	Peak flow relative error/E%	The coefficient of water balance/W	Peak flow time error/T(h)
2008060 90000	rain gauge	0.8	0.91	15	3	0.89	-6
	PERSIANN-CCS QPEs	0.6	0.65	26	36	0.83	-69
	the post-processed PERSIANN-CCS QPEs	0.63	0.73	21	6	0.92	-60
2009060 90800	rain gauge	0.95	0.92	17	4	0.9	-12
	PERSIANN-CCS QPEs	0.67	0.61	28	34	0.79	-36
	the post-processed PERSIANN-CCS QPEs	0.75	0.64	22	14	0.85	-30
2011060	rain gauge	0.8	0.84	16	3	1.02	-7

10900	PERSIANN-CCS QPEs	0.65	0.83	25	21	0.89	-17
	the post-processed PERSIANN-CCS QPEs	0.75	0.85	21	12	0.92	-12
2012060 2200	rain gauge	0.82	0.79	20	5	0.8	-6
	PERSIANN-CCS QPEs	0.69	0.54	31	17	0.75	-21
	the post-processed PERSIANN-CCS QPEs	0.71	0.74	23	12	0.78	-15
2013060 11400	rain gauge	0.95	0.82	20	6	0.92	-4
	PERSIANN-CCS QPEs	0.7	0.84	28	10	0.79	-15
	the post-processed PERSIANN-CCS QPEs	0.82	0.89	24	7	0.85	-10
average value	rain gauge	0.86	0.86	18	4	0.91	-7
	PERSIANN-CCS QPEs	0.66	0.69	28	24	0.81	-32
	the post-processed PERSIANN-CCS QPEs	0.73	0.77	22	10	0.86	-25

874   Table 4. Evaluation indices of simulated flood events with different model parameters

flood	Parameter type	Nash-Sutcliffe coefficient/C	Correlation coefficient/R	Process relative error/P %	Peak flow relative error/E%	The coefficient of water balance/W	Peak flow time error/T(h)
2008060	rain gauge	0.8	0.91	15	3	0.89	-6

90000	Coupling model/the same model parameters as rain gauges	0.63	0.73	21	6	0.92	-60
	Coupling model/re-optimized model parameters	0.76	0.83	18	5	0.93	-4
2009060 90800	rain gauge	0.95	0.92	17	4	0.9	-12
	Coupling model/the same model parameters as rain gauges	0.75	0.64	22	14	0.85	-30
	Coupling model/re-optimized model parameters	0.82	0.78	19	7	0.87	-5
2011060 10900	rain gauge	0.8	0.84	16	3	1.02	-7
	Coupling model/the same model parameters as rain gauges	0.75	0.85	21	12	0.92	-12
	Coupling model/re-optimized model parameters	0.78	0.87	19	6	0.94	-10
2012060 2200	rain gauge	0.82	0.79	20	5	0.8	-6
	Coupling model/the same model parameters as rain gauges	0.71	0.74	23	12	0.78	-15
	Coupling model/re-optimized model parameters	0.78	0.76	21	8	0.79	-10
2013060	rain gauge	0.95	0.82	20	6	0.92	-4

11400	Coupling model/the same model parameters as rain gauges	0.82	0.89	24	7	0.85	-10
	Coupling model/re-optimized model parameters	0.86	0.91	22	6	0.87	-8
average value	rain gauge	0.86	0.86	18	4	0.91	-7
	Coupling model/the same model parameters as rain gauges	0.73	0.77	22	10	0.86	-25
	Coupling model/re-optimized model parameters	0.8	0.83	20	6	0.88	-7

References

876 Abbott, M. B., Bathurst, J. C., Cunge, J. A., O'Connell, P. E.,and Rasmussen, J.: An Introduction to the

877 European HydrologicSystem-System Hydrologue Europeen, 'SHE', a: History and Philosophy of a

878 Physically-based, Distributed Modelling System,J. Hydrol., 87, 45–59, 1986a.

879 Abbott, M. B.,Bathurst, J. C.,Cunge, J. A.,O'Connell, P. E., and Rasmussen, J.: An Introduction to the

880 European Hydrologic System-System Hydrologue Europeen, 'SHE', b: Structure of a Physically based,

881 distributed modeling System, J. Hydrol., 87,61–77, 1986b.

882 Ambroise, B., Beven, K., and Freer, J.: Toward a generalization of the TOPMODEL concepts:

883 Topographic indices of hydrologic similarity, Water Resour. Res., 32,2135–2145, 1996.

884 Ashouri, H., Hsu, K.L., Soroosh,S., Braithwaite, D. K., Knapp, K. R., and Cecil, L. D.: PERSIANN-
885 CDR: Daily Precipitation Climate Data Record from Multisatellite Observations for Hydrological and
886 Climate Studies. Bulletin of the American Meteorological Society, 96(1):197-210, 2014.

887 Atkinson, T.C.: Diffuse flow and conduit flow in limestone terrain in the Mendip Hills, Somerset
888 (Great Britain). Journal of Hydrology, 35(1-2):93-110, 1977.

889 Bartsotas, N., Nikolopoulos, E., Anagnostou, E., and Kallos, G.: Improving satellite quantitative
890 precipitation estimates through the use of high-resolution numerical weather predictions: Similarities
891 and contrasts between the Alps and Blue Nile region// EGU General Assembly Conference. EGU
892 General Assembly Conference Abstracts, 2017.

893 Birk,S., Geyer, T., Liedl, R., and Sauter, M.: Process-based interpretation of tracer tests in carbonate
894 aquifers. Ground Water, 43(3): 381-388, 2005.

895   Chen, Y.B, Li, J., Wang, H., Qin, J., and Dong, L.: Large-watershed flood forecasting with high-
896   resolution distributed hydrological model, Hydrol. Earth Syst. Sci., 21, 735–749, doi:10.5194/hess-21-
897   735-2017, 2017.

898   Chen, Y.B., Li, J., and Xu, H.J.: Improving flood forecasting capability of physically based distributed
899   hydrological models by parameter optimization, Hydrol. Earth Syst. Sci., 20, 375–392,
900   doi:10.5194/hess-20-375-2016, 2016.

901   Chen, Y.B.: Liuxihe Model, China Science and Technology Press, Peking, China, September 2009.

902   Davis W.M.: Relation of geography to geology. Geological Society of America Bulletin, 23,1912.

903   Delrieu,G., Bonnifait, L., Kirstetter, P. E., and Boudevillain, B.: Dependence of radar quantitative
904   precipitation estimation error on the rain intensity in the Cévennes region, France. Hydrological
905   Sciences Journal, 59(7):1308-1319,2014.

906   Doummar, J., Margane, A., Sauter, M., and Geyer, T.: Assessment of transport parameters in a karst
907   system under various flow periods through extensive analysis of artificial tracer tests// EGU General
908   Assembly Conference. EGU General Assembly Conference Abstracts, 2012.

909   Duan, J.,and Miller,N.L.: A generalized power function for the subsurface transmissivity profile in
910   TOPMODEL. Water Resources Research, 33(11):2559–2562, 1997.

911   Falorni, G., Teles, V., Vivoni, E. R., Bras, R. L., and Amaratunga, K. S.: Analysis and characterization
912   of the vertical accuracy of digital elevation models from the Shuttle RadarTopography Mission, J.
913   Geophys. Res.-Earth, 110, F02005, doi:10.1029/2003JF000113, 2005.

914   Faure, D., Gaussiat, N., Tabary, P., and Urban, B.: Real time integration of foreign radar quantitative
915   precipitation estimations (QPEs) in the French national QPE mosaic// Conference on Radar
916   Meteorology, AMS,21-21, 2015.

917   Ford, D., and Williams P.W.: Karst Geomorphology and Hydrology. Geographical Journal,
918   157(1):87,1991.

919   Freeze, R. A. and Harlan, R. L.: Blueprint for a physically-based,digitally simulated, hydrologic
920   response model, J. Hydrology., 9,237–258, 1969.

921   Goldscheider, N., and Drew, D.: Methods in Karst Hydrogeology: IAH:International Contributions to
922   Hydrogeology, 26. CRC Press, 2007.

923   Goudenhoofdt E, Delobbe L.: Evaluation of radar-gauge merging methods for quantitative precipitation
924   estimates. Hydrology & Earth System Sciences, 13(2):195-203.,2009.

925   Hartmann, A., Barberá J. A., Lange, J., Andreo, B., and Weiler, M.: Progress in the hydrologic
926   simulation of time variant recharge areas of karst systems – Exemplified at a karst spring in Southern
927   Spain. Advances in Water Resources, 54(2):149-160, 2013.

928   Hirpa, F. A., Gebremichael, M., and Hopson, T.: Evaluation of high-resolution satellite precipitation
929   products over very complex terrain in ethiopia. J.appl.meteor.climatol, 49(5), 1044-1051.,2010.

930   Hsu, K. L., Gupta, H. V., Gao, X.G, and Soroosh,S.: Estimation of physical variables from
931   multichannel remotely sensed imagery using a neural network: Application to rainfall estimation.
932   Water Resources Research, 35(5):1605-1618,1999.

933 Hsu, K.L, Yang,H., and Soroosh,S.: Rainfall Estimation Using a Cloud Patch Classification Map//
934 Measuring Precipitation From Space. Springer Netherlands,329-342, 2007.

935 Hussain, Y., Satgé, F., Hussain, M. B., Martinez-Carvajal, H., Bonnet, M. P., and Cárdenas-Soto, M.:
936 Performance of CMORPH, TMPA, and PERSIANN rainfall datasets over plain, mountainous, and
937 glacial regions of Pakistan. Theoretical & Applied Climatology, 131(3-4), 1119-1132,2018.

938 Hu, Q.F., Yang,D.W.,Wang,Y.T.,Yang,H.B.,and Liu,Y.: Characteristics and sources of errors in daily
939 TRMM precipitation product over Ganjiang River basin in China. ADVANCES IN WATER
940 SCIENCE,24(6):794-800,2013.

941 Kovacs,A., and Perrochet,P.: Hydrograph Analysis for Parameter Estimation of Connected and Karst
942 Systems// Engineers Australia, 2011.

943 Li, J., Chen, Y.B., Wang, H.Y., Qin, J.M., Li, J., and Chiao, S.: Extending flood forecasting lead time
944 in a large watershed by coupling WRF QPF with a distributed hydrological model. Hydrology & Earth
945 System Sciences Discussions, 21:1-45,2017.

946 Li,B.G.,and Tao,S.: Several Problems and Their Solutions in Surface Runoff Modeling. Bulletin of Soil
947 and Water Conservation, 20(3):47-49,2000.

948 Li,G.F.: Karst Hydrogeologic Characteristics and Water Resources in Guangxi,China, Carsologica
949 Sinica,3:253-258,1996.

950 Li,X.M., and Ren,B.: The calculation method of non-closure small watershed of the mine water runoff
951 in ungauged basins. Mineral Engineering Research, 2009.

952 Liu,H.M.Deng,H.P.,Sun,S.F.,and Xiao,Y.: .Numerically Test of Influence of Incorporation of
953 TOPMODEL into Land Surface Model SSiB on Hydrological Simulation at Basin Scale.PLATEAU
954 METEOROLOGY, 32(3):829-838,2013.

955 Liu, X.Y.,Yang, T., Hsu ,K.L., Liu, C., and Soroosh,S.: Evaluating the streamflow simulation
956 capability of PERSIANN-CDR daily rainfall products in two river basins on the Tibetan Plateau.
957 Hydrology & Earth System Sciences Discussions, 21(1):1-31, 2017.

958 Loveland, T. R., Merchant, J. W., Ohlen, D. O., and Brown, J. F.: Development of a Land Cover
959 Characteristics Data Base for the Conterminous U.S., Photogram, Photogramm. Eng. Rem. S., 57,
960 1453–1463, 1991.

961 Loveland, T. R., Reed, B. C., Brown, J. F., Ohlen, D. O., Zhu, J., Yang, L., and Merchant, J. W.:
962 Development of a Global Land Cover Characteristics Database and IGBP DISCover from 1-km
963 AVHRR Data, Int. J. Remote Sens., 21, 1303–1330, 2000.

964 Liang,H.: Prelim in Ary Study on the Characteristics of Flood Discharge and Low Flow in Fluenced by
965 the Scale of Karst Dranin Age Basin- Exampled by the River s in Guizhou Province,China, Carsologica
966 Sinica. 2:121-129, 1997.

967 Moradkhani, and Meskele, T.T.: Satellite Rainfall Applications for Surface Hydrology. Springer
968 Netherlands, 2010.

969 Neitsch,S.L.,J.G.Arnold,J.R.Kiniry and J.R.Williams.: Soil and Water Assessment Tool
970 Theoretical Documentation Version,2000.

971 Quinlan, J.F and Ewers, R.O.: Ground water flow in limestone terranes -strategy, rationale and
972 procedure for reliable, efficient monitoring of ground water in karst areas. Mendeley, 8:167-173, 1985.

973 Quinlan, J. F., Davies, G. J., Jones, S. W., and Huntoon, P. W.: The applicability of numerical models
974 to adequately characterize ground-water flow in karstic and other triple-porosity aquifers. 1288:114-

133, 2011.

Rafieei,N.A., Norouzi,, A., Kim, B., and Seo, D.: J Fusion of multiple radar-based quantitative precipitation estimates (QPE) for high-resolution flash flood forecasting in large urban areas// AGU Fall Meeting. AGU Fall Meeting Abstracts, 2014.

Ren,Q.W.: Water Quantity Evaluation Methodology Based on Modified SWAT Hydrological Modeling in Southwest Karst Area. China University of Geoscience, Wuhan ,China, 2006.

Romill, T. G. and Gebremichael, M.: Evaluation of satellite rainfall estimates over Ethiopian river basins. Hydrol. Earth Syst. Sci., 15, 1505–1514, 2011, doi:10.5194/hess-15-1505-2011.

Saxton, K.E, Rawls, W. J, Romberger, J .S, and Papendick, R. I.: Estimating generalized soil water characteristics from texture. Soil Science Society of America Journal, 50: 1031- 1036,1986.

Servat, E .,and Sakho,M.: Modelling and management of sustainable basin-scale water resource systems : proceedings of an international symposium held at Boulder, Proceedings of IAHS Symposium 6, IAHS Publication No.231,1995.

Sharma, A. and Tiwari, K. N.: A comparative appraisal of hydrological behavior of SRTM DEM at catchment level, J. Hydrol., 519, 1394–1404, 2014.

Shuster, E .T, and White,W.B.: Seasonal fluctuations in the chemistry of lime-stone springs: A possible means for characterizing carbonate aquifers. Journal of Hydrology, 14(2):93-128,1971.

Soroosh,S., Hsu ,K.L.,Gao,,X.G.,Hoshin,V.G.,Bisher,I.,and Braithwaite, D.: Evaluation of PERSIANN System Satellite-Based Estimates of Tropical Rainfall. Bulletin of the American Meteorological Society,81,2035-2046,2000.

Stenz, R.D.: Improving satellite quantitative precipitation estimates by incorporating deep convective cloud optical depth. Dissertations & Theses - Gradworks, 2014.

Strahler, A. N.: Quantitative analysis of watershed Geomorphology,Transactions of the American Geophysical Union, 35, 913–920,1957.

Tan ,M.L., and Santo,H.: Comparison of GPM IMERG, TMPA 3B42 and PERSIANN-CDR satellite precipitation products over Malaysia. Atmospheric Research, , 202, 2018.

Wardhana A, Pawitan H, and Dasanto B D.: Application of hourly radar-gauge merging method for quantitative precipitation estimates//012033,2017.

Williams,P.W.: Geomorohic inheritance and the development of tower karst Earth surface Progresses and landform.12,453-465,1987.

Yang,H., Hsu, K. L., Soroosh,S., and Gao, X.G.: Precipitation Estimation from Remotely Sensed Imagery Using an Artificial Neural Network Cloud Classification System. Journal of Applied Meteorology, 36(9):1176-1190,2004.

Yang,H.,Gochis, D., Cheng, J. T., Hsu, K. L., and Soroosh,S.: Evaluation of PERSIANN-CCS Rainfall Measurement Using the NAME Event Rain Gauge Network. Journal of Hydrometeorology, 8(3):469, 2007.

Zhang,C.,Jiang,Y.J.,Lian,Y.Q.,Yuan,D.X.,Pei,J.G.,and Jiang,G.H.: Rainfall-runoff simulation of a typical karst fengcong depression system using SWMM model-A case study of the Yaji experimental site in Guilin.Hydrogeology and Engineering Geology,34(3):10-14, 2007.